



A novel coaxial powder-feeding additive friction stir deposition method and its application in the recycling of nylon waste fine powder

Zhongxu Liu¹ · Wenguang Nan¹ · Ziming He¹ · Zhonggang Sun¹ · Wenya Li²

Received: 24 February 2025 / Accepted: 7 May 2025

© The Author(s), under exclusive licence to Springer Nature Switzerland AG 2025

Abstract

A novel powder-based additive friction stir deposition (AFSD) with coaxial powder feeding is proposed in this work, in which the material can be continuously fed without any blocking/chocking problem, and the feeding rate of fine powder could be easily controlled by the rotating screw. The plastic deformation of powder material in this method is mainly due to the friction stir effect of the rotating tool instead of the screw extrusion. The feasibility of this method in the recycling of nylon 6 powder with different size classes is demonstrated. The manufactured specimen has no significant defects except for the ripple skin and flashes at the edges, which are also prone in other kinds of AFSD. The deposition temperature of the powder material is around 75% of the melting temperature. The material extruded from the channel between the protrusions of the tool moves at a very slow speed (i.e. 2–3 mm/s) before being deposited onto the base, which is only a few percent of the rotational speed of the tool. The α -type crystals are prone to forming in the manufactured specimens for all kinds of powder used in this work, although the experiment is conducted under natural cooling conditions at room temperature. The high hardness of the specimen, i.e. 160–200 MPa, demonstrates the advantage of the additive friction stir deposition developed in this work. The mechanical performance of the specimen increases with the particle size of the powder as they are more easily plastically deformed under the friction stir effect of the tool.

Keywords Additive friction stir deposition · Solid-state additive manufacturing · Cohesive powder · Screw feeding · Coaxial powder feeding · Recycling

1 Introduction

In recent years, thermoplastic materials have been widely utilised in additive manufacturing due to their excellent mechanical properties, heat resistance, and corrosion resistance, particularly in powder bed fusion (PBF) technology.

The PBF process employs high-energy sources such as laser or electron beams to scan the powder bed layer by layer, enabling the precise fabrication of complex structures. Unlike conventional melt-based additive manufacturing techniques, additive friction stir deposition (AFSD) [1, 2] provides a promising solution for the efficient manufacturing of thermoplastic materials, in which a rotating tool is employed to generate frictional heat and pressure [3, 4], causing the raw material to undergo plastic deformation in the solid state and deposit onto the substrate. During this process, the material remains in the solid phase without undergoing melting, thereby avoiding phase transitions and eliminating defects such as porosity and cracking during the melting-solidification processes as occurred in PBF [5, 6], resulting in the good quality and performance of fabricated components [7, 8].

In AFSD, the feeding materials could range from rods [9, 10] and wires [11, 12] to chips [13, 14] and even powder [15, 16]. Compared to rod-based AFSD, in the wire/chips/powder-based AFSD, the material could be continuously fed

✉ Wenguang Nan
nanwg@njtech.edu.cn

✉ Zhonggang Sun
sunzgg@njtech.edu.cn

Zhongxu Liu
202361207210@njtech.edu.cn

Ziming He
heziming2023@njtech.edu.cn

Wenya Li
liwy@nwpu.edu.cn

¹ Nanjing Tech University, Nanjing, China

² Northwestern Polytechnical University, Xi'an, China

without any break. In the wire-based AFSD as proposed by Chen et al. [17] and Zhang et al. [18], a specifically designed screw was used to convey and cut the wires into large particles and then extrude them into deposited layers, while the stirring probes on the head of the screw could accelerate the fluidity of the thermo-plasticised materials and improve the bonding between the adjacent layers. They showed that the deposited layer could achieve 111% of wire base metal in terms of ultimate tensile strength, in which the Al–Si alloy wire with a diameter of 2.4 mm was used. Jordon et al. [19] proposed a novel method for recovering and reusing metal machine chips via the AFSD process, in which the aluminium alloy 5083 plates were cut into chips with a length of 2–3 mm using a mill. In their chips-based AFSD, a screw or an auger was used to push and consolidate the chips to flow through a hollow rotating tool and deposit onto a substrate and subsequent layers. Similar system was also reported in their another recent work [20], in which a high performance of the specimen was reported. It should be noted that in chips-based AFSD, the material is usually already plastically deformed from chips into a semi-solid state under the action of the screw before being further processed by the rotating tool. Recently, this concept has been successfully extended to the screw extrusion of large-sized particles, as reported by Zhang et al. [21], in which 2 mm pure aluminium particles cut from wires were used. Although AFSD has made significant progress in processing materials in rod, wire, and chip forms, minor work is available for the AFSD methods applicable for fine powder.

Compared to other methods, the material in powder-based AFSD does not have restrictive requirements on the shape and size like the rods or wires or chips or specifically manufactured large particles, and the waste powder collected from the industry or the commercial powder already available in the industry could be all used. Chaudhary et al. [22] used pressurised carrier gas for the first time to continuously discharge the material from the powder feeder to the substrate through the hollow tool, which has a hole of 3 mm diameter to facilitate the flow of the deposition powder. Due to the ability of gas conveying, very fine powder was used in the experiment, i.e. 40–100 μm 6061 Al alloy powder. By using this method, they produced a single layer with a maximum height of 0.45 mm. Besides this gas coaxial feeding process, external feeding was innovatively proposed by Mukhopadhyay [23] to avoid the blockage problem. Mukhopadhyay [23] directly used a compressor and duct to continuously feed powder from a container to the working zone, in which the powder is poured externally in front of the tool instead of feeding through the hollow tool, and 50–300 μm pure aluminium powder was used in their experiment. To avoid the ejection of the powder on the smooth substrate, they used a substrate with a shallow groove (3mm in depth) dug on it. This system was also followed by Chaudhary et al. [15, 24],

and recently improved by Mukhopadhyay et al. [25]. These pieces of work demonstrated the feasibility of the development of powder-based AFSD; however, the robustness of the powder feeding system and its application to the engineering plastics powder, such as nylon, PC and ABS, is still questionable. Meanwhile, the powder-based AFSD with coaxial feeding is only reported by Chaudhary et al. [22], but the gas-feeding system is too complex, and it is usually only suitable for fine powder.

In this work, a new kind of powder-based AFSD system with coaxial powder feeding is proposed and developed, in which the deformation of the particles of the powder only arises from the friction stir effect of the rotating tool rather than from screw extrusion, thereby avoiding the risk of choke at the funnel outlet and extending the variety of the feeding material for AFSD technique. Then, it is applied to recycle the nylon 6 powder with different size classes to demonstrate its low requirements for powder size and its advantages than conventional recycling methods. The quality of the specimen, such as its morphology, thermodynamic and mechanical properties, crystal structure, as well as the temperature and flow pattern of the powder material during the deposition process, are examined. These results will have a notable impact on the development of powder-based AFSD and its application on the recycling of nylon powder.

2 Methods

2.1 Set-up of experiments

The schematics and snapshots of the powder-based additive friction stir deposition (AFSD) system developed in this work are shown in Fig. 1. Here, the rotating tool with a hole in the middle is assembled with a coaxial powder feeding system, and they are together supported by a slide rail with a reciprocating motion in X direction. The clearance between the tool bottom and the work surface, i.e. the layer thickness, is precisely controlled by adjusting the vertical position of the work surface through an electric cylinder with linear bearings, which has a resolution of 0.01 mm and a rated pushing force of 2.5 kN. The rotational motion of the tool is realised by using a synchronous pulley system. The continuous powder feeding is conducted by a rotating screw with a diameter of 14 mm, which is surrounded by a coaxial funnel with an inner diameter of 16 mm. The rotational motion of the screw is controlled by a servo motor of 0.75 kW and a speed reducer with a gear ratio of 10. To monitor the temperature of the material during the deposition process, an infrared thermal imager with a resolution of 256×192 (Hikvision Digital Technology Co., Ltd) is placed in front of the work surface. To keep up the vertical position of the work surface when multi-layers are deposited, the infrared

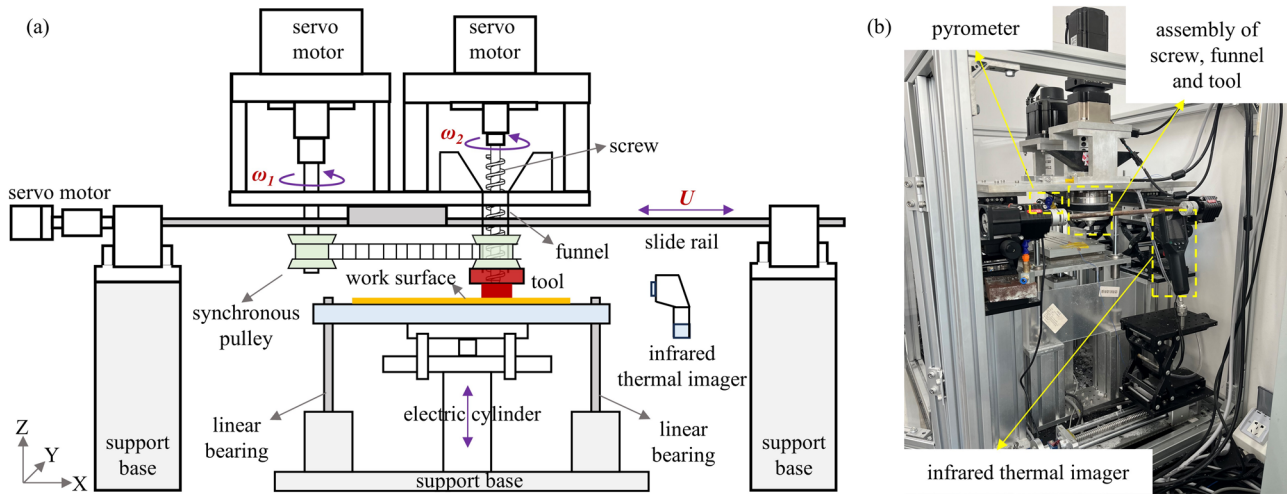


Fig. 1 Set-up of the powder-based additive friction stir deposition system: **a** schematics of the experiment system, including a coaxial powder feeding system using a screw with a rotational speed of ω_2 , a rotating tool with a rotational speed of ω_1 , a slide rail system with

a travelling speed of U , and an electric cylinder to control the vertical position of work surface; **b** snapshots of the experiment system, including an infrared thermal imager and a pyrometer

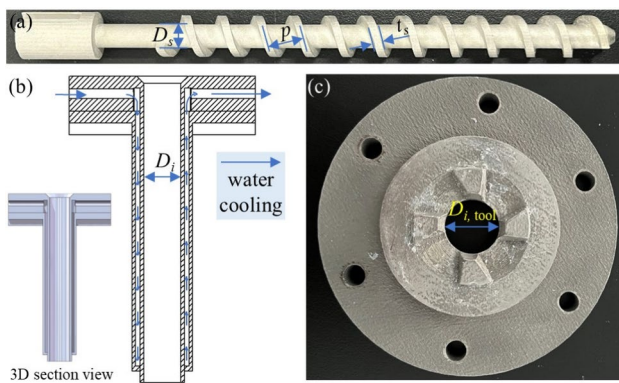


Fig. 2 Key parts of the experiment system: **a** snapshots of the screw; **b** 2D and 3D drawings of the funnel, in which the water flow is used to cool the feeding process of the screw; **c** snapshots of the tool, in which four protrusions are manufactured; the key parameters are also labelled: $D_{i,tool}$ is the diameter of the hole of the tool, D_i and D_s are the inner diameter of the funnel and the diameter of the shaft of the screw, respectively, p is the pitch of the screw, t_s is the thickness of the blade of the screw

thermal imager is fixed with a lifter platform with a resolution of 0.1 mm. It should be noted that the thermal image is only collected when the tool moves back to the specified position from the rightmost side. Meanwhile, a pyrometer is also used to monitor the temperature of the work surface to assist in debugging process parameters.

2.2 Concepts of powder-based AFSD

The key parts of the experimental system are shown in Fig. 2. The screw is manufactured from 316L stainless steel,

and the pitch is 9 mm with a total length of 144 mm, as shown in Fig. 2a. The blade has a thickness of 3 mm, and the diameter of the shaft is 8 mm. The theoretic maximum volumetric feeding rate of the screw $Q_{th,screw}$ is given as [26]:

$$Q_{th,screw} = \frac{\pi}{4} (D_i^2 - D_s^2) \cdot (p - t_s) \cdot \frac{\omega_2}{60} \cdot \phi_{avg} \quad (1)$$

where D_i and D_s are the inner diameter of the funnel and the diameter of the shaft of the screw, respectively, as shown in Fig. 2; p is the pitch of the screw; t_s is the thickness of the blade of the screw; ω_2 is the rotational speed of the screw, which is in the unit of rpm; ϕ_{avg} is the averaged particle fraction, and the value of 0.5 is used here for reference. The theoretical maximum volumetric feeding rate could be further normalised by the flow area of the inner hole of the tool, given as:

$$\bar{Q}_{th,screw} = \frac{\frac{\pi}{4} (D_i^2 - D_s^2) \cdot (p - t_s) \cdot \frac{\omega_2}{60} \cdot \phi_{avg}}{\frac{\pi}{4} D_{i,tool}^2} \quad (2)$$

where $D_{i,tool}$ is the diameter of the hole of the tool. According to the geometric parameters of the screw and the tool used in the experiment, the variation of the normalised theoretic maximum volumetric feeding rate with the rotational speed of the screw is shown in Fig. 3. It should be noted that for the realistic feeding rate of the screw, the packing fraction in Eq. (2) varies with powder properties and the rotational speed of the screw. Meanwhile, the constraints of the outlet of the feeding system also affects the feeding rate of the screw in powder-based AFSD, as reported by the author's previous work [27], resulting in the feeding rate not being possible accurately predicted by the traditional theory

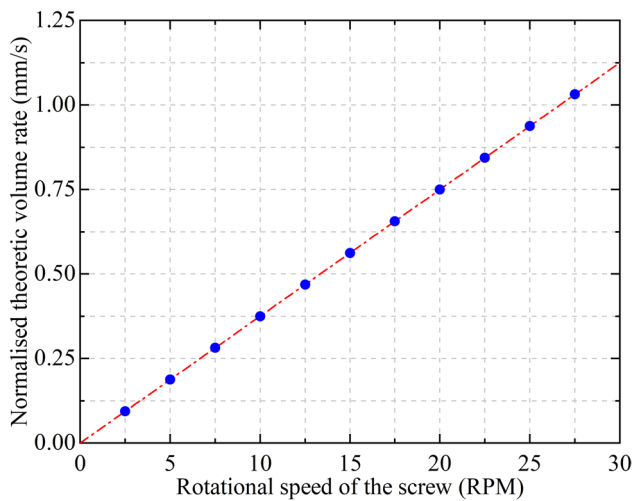


Fig. 3 Variation of the normalised theoretical maximum volumetric feeding rate of the screw used in the experiment with the rotational speed of the screw

of screw feeding. This brings a challenge to the accurate control of the feeding rate of materials, which is much different from that of rod-based AFSD.

For the funnel surrounding the screw, it is specifically designed, as shown in Fig. 2b, in which a water channel is adopted. In reality, the inner wall of the funnel may be heated by the heat conducted upwards from the tool. By using the funnel developed in this work, the inner wall of the funnel could be well-cooled by water flow to ensure that the powder is not at a high temperature. In this way, the flowability of the powder could be well guaranteed throughout the whole AFSD process, especially for fine powder. It should be noted that the feeding system, i.e. the screw and funnel, is only used to feed powder into the tool region instead of severely deforming the particles into softened materials.

This is easily clarified by suddenly stopping the deposition process and only discrete particles are observed at the region of the bottom of the funnel. As shown in Fig. 2c, the tool has four protrusions adjacent to the inner hole with a diameter of 16 mm. The diameter of the bottom of the tool is 52 mm, while the diameter of the outer side of the protrusions is 34 mm.

Before the experiment, the electric cylinder moves upward to bring the substrate into contact with the tool, and the contact point, which is represented by the sudden increase of the pushing force of the electric cylinder, is assigned as the zero position of the work surface or the substrate. Then the tool begins to rotate at a constant rotational speed and the substrate is further pushed upward to let the protrusions of the tool penetrate into it, as shown in Fig. 4a. Meanwhile, the slide rail supporting the tool begins to move at a constant speed, causing the tool to rub and stir the substrate. In this way, under the combined effect of the plastic deformation of the substrate surface and the intense friction between the tool and substrate, the tool is pre-heated to the desired temperature.

After the preheating phase, the powder is poured into the funnel by a hopper above it. Then the screw begins to rotate at a constant rotational speed, and the powder is fed through the hole of the tool and pushed into the clearance between the tool bottom and worksurface. Under the effect of the heat accumulated in the preheating process, the particles easily undergo severe plastic deformation as induced by the action of the tool. Under the impact of the centrifugal force generated by the tool's rotation, the deformed material is extruded out through the flow channels between the tool protrusions and deposits at the retreating side of the tool as the tool moves forward, as shown in Fig. 4b.

After each deposition cycle, the worksurface would be lowered by a constant distance through the linear motion

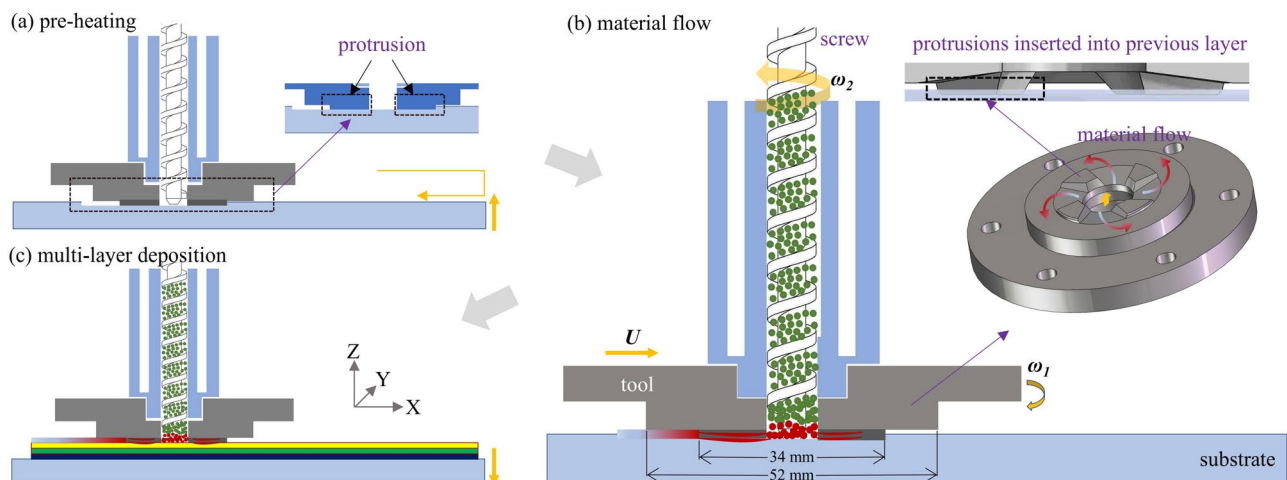


Fig. 4 Procedures of the powder-based AFSD developed in this work, including **a** pre-heating, **b** material flow and **c** multi-layer deposition

of the electric cylinder. It should be noted that this constant distance should be smaller than the height of the protrusion. In this way, in each deposition cycle, the protrusions of the tool are penetrated into the previously manufactured layer, as shown in Fig. 4c. Under the reciprocating movement of the slide rail system supporting the tool and feeding system and the periodic downward movement of the electric cylinder, a multi-deposition layer could be gradually achieved.

This new kind of powder-based AFSD system proposed and developed in this work outperforms traditional rod-based or extrusion-based AFSD and previously immature powder-based AFSD, such as more flexible than the rod-based AFSD in terms of material feeding and material variety, much less requirement on the particle size than the extrusion-based AFSD, while avoiding the disadvantages of the previously AFSD based on fine powder, such as the blocking/choke problem using gas feeding in Chaudhary et al. [22] and the inflexibility problem using external feeding in Mukhopadhyay [23]. Therefore, it could be applicable to the raw powder from industry without the fabrication of the rod bars or the granulation of large particles, and it has low requirements on the powder size and the stiffness of the powder material. Meanwhile, it is environmentally friendly, as the manufacturing is conducted at the temperature below the melting point of powder material, avoiding the risk of the release of polluted gases or smells.

2.3 Materials

To address the feasibility of the system developed in this work on the recycling of powder, nylon 6 powder is used in this work. The particle shape of the powder is irregular, as observed from the SEM image shown in Fig. 5a. To further address that the powder used in this system does

not have much restrictions on the particle size, the original nylon 6 powder is further sieved into three kinds of size classes using the sieves obeying ASTM E 11–87 and the particle size distribution is measured by Mastersizer 2000 (Malvern Instruments Ltd, UK), as shown in Fig. 5b and summarised in Table 1: (1) powder A, the volume-based particle size is $d_{50}=0.258$ mm, which is sieved from No. 100 and No. 50 sieves; (2) powder B, the volume-based particle size is $d_{50}=0.488$ mm, which is sieved from No. 50 and No. 35 sieves; (3) powder C, the volume-based particle size is $d_{50}=0.791$ mm, which is sieved from No. 35 and No. 20 sieves.

The apparent density of the powder is measured at room temperature based on the ASTM B213 test procedure. It is 0.506, 0.555 and 0.573 g/cm³ for powders A, B and C, respectively, indicating that powder could have a larger apparent density with the increase of particle size. The flowability of these powders at room temperature is characterised by the dynamic repose angle, as measured by the drum developed in-house, in which the inner diameter of the drum is 80 mm. A larger repose angle indicates a worse flowability. Here, the maximum angle between the slopes of the linearised fit of the right and left part of the free surface of particle flow in the drum is used to represent the

Table 1 Physical properties of powder used in the experiment

Powder label	Apparent density (g/cm ³)	Particle size d_{50} (mm)	Dynamic repose angle (°)
Powder A	0.506	0.258	59.8
Powder B	0.555	0.488	50.6
Powder C	0.573	0.791	46.6

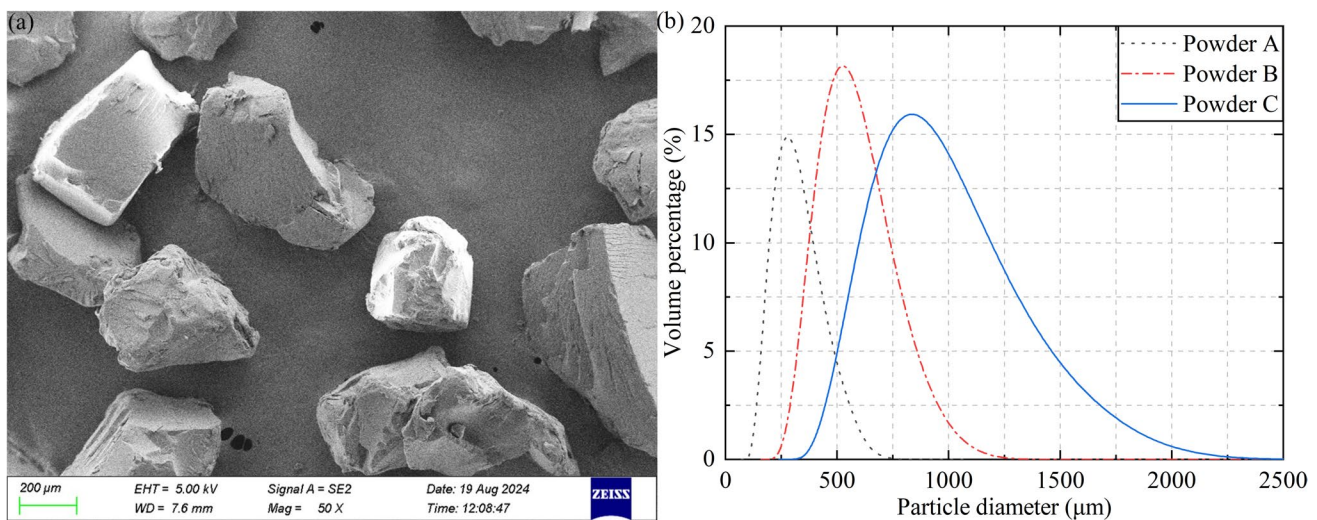


Fig. 5 Powder used in the experiment: **a** SEM image of particles and **b** volume-based particle size distribution

dynamic repose angle. The rotational speed of the drum is 10 rpm during the characterisation test. The dynamic repose angles of powders A, B and C are 59.8° , 50.6° and 46.6° , respectively. It suggests that as the particle size decreases, the flowability of the powder becomes worse, which is intuitively expected. It also agrees well with the apparent density, i.e. the powder with worse flowability has a smaller apparent density.

In the experiment, as reported in this work, the rotational speed of the tool is 1200 rpm, while its translational speed, as controlled by the slide rail, is 3.2 mm/s, and the layer thickness is 0.6 mm. Considering the difference in the apparent density and flowability of powders, a larger rotational speed of the screw is used for the powder with a smaller particle size, i.e. 27.5, 22.5 and 17.5 rpm for powder A, powder B and powder C, respectively, as summarised in Table 2. The process parameters used in this work have been well adjusted and optimised after a long time of trial tests, thus, the effect of process parameters (e.g. rotational speed of tool,

layer thickness) on the deposition quality is not focussed in this work.

3 Results and discussions

3.1 Morphology and depositing features

Figure 6 shows the snapshots of the specimen as manufactured from the powder-based AFSD method developed in this work, including a naked-eye observation of the whole specimen and a zoom-out view of the specimen surface using a camera with a resolution of 2600×2160 pixels (a2A2600-64umBAS, Basler AG, Germany). The maximum thickness of the specimen is approximately 15 mm. The width of the specimen along the advancing direction of the tool is uniform, indicating that the feeding rate through the screw and the heat generation by the rotating tool is well controlled during the whole deposition process. The width of the specimen is around 40 mm, which is between the diameters of the protrusions (i.e. 34 mm) and the shoulder (i.e. 52 mm) of the tool. This correlates well with the infrared thermal image, as shown in Fig. 7. The region with a high temperature represents the material located between the tool and the work surface, and its width is smaller than the diameter of the tool shoulder ($D_{tool} = 52$ mm). The material in this region is plastically deformed under the friction stir effect of the tool. It should be noted that the material is mainly deformed in this region, as inferred from Fig. 8. Figure 8 shows that after the manufacturing process, both the screw and the funnel do not need to be carefully cleaned, i.e. there is no plastically deformed powder strongly adhered to the

Table 2 Process parameters used in the experiment

Parameters	Value
Rotational speed of the tool, ω_1 (rpm)	1200
Rotational speed of the screw, ω_2 (rpm)	27.5 ^{*a} , 22.5 ^{*b} , 17.5 ^{*c}
Translational speed, U (mm/s)	3.2
Layer thickness (mm)	0.6

*The value with the superscripts of a, b and c represents the screw rotational speed adopted by powder A, powder B and powder C, respectively

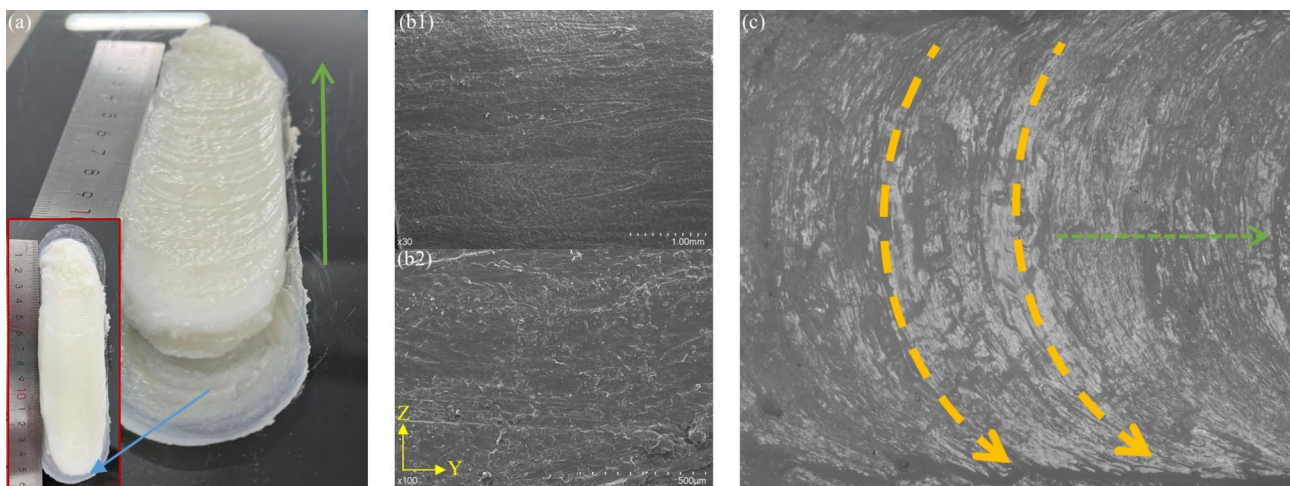


Fig. 6 Snapshots of the specimen as manufactured from powder-based AFSD: **a** naked-eye observations of the whole specimen; **b** cross-section along the vertical direction as observed using SEM with magnification ratios of 30 and 100; **c** “ripple skin” as observed

using a Basler camera, in which the green arrows indicate the advancing direction of the tool in the last deposition routine and the orange arrows indicate the rotational direction of the tool

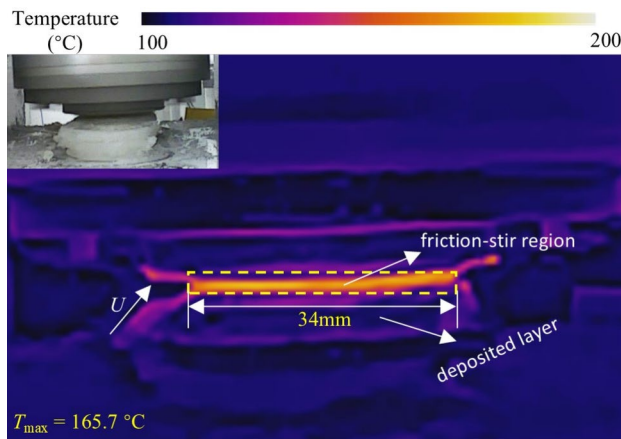


Fig. 7 Infrared thermal image of the material flow between the tool and previously deposited layer, in which the corresponding visible light picture is also enclosed, and the friction-stir region has the same diameter of the outer edge of the tool protrusions while its maximum temperature is 165.7 °C

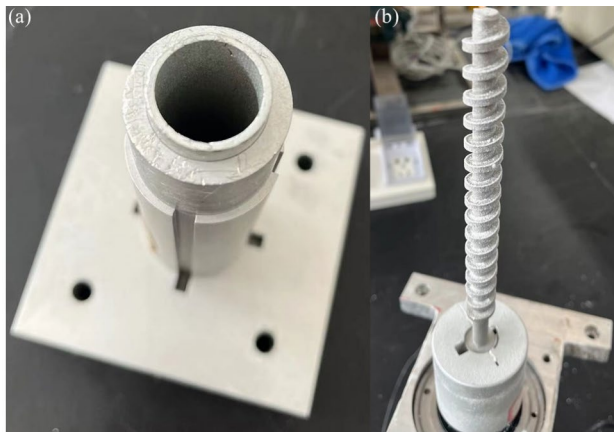


Fig. 8 Observations of **a** the funnel outlet and **b** the screw after the experiment, in which no plastically deformed powder is observed to strongly adhere to the screw or block the funnel outlet

screw, and no softened materials are blocking the funnel outlet. This is different from the systems reported by Jordon et al. [19] and Beck et al. [20], where the large particles or chips are already plastically deformed in the funnel under the interaction between the particles and the screw before being pushed out of the funnel, and they are further plastically deformed when depositing onto the base.

Figure 7 also shows that the temperature of the material during the deposition process is below the melting temperature (i.e. around 220 °C for nylon 6 used in this work). This agrees well with the nature of solid-state additive manufacturing [28, 29], which could avoid the defects produced in other AM methods with melting and solidification processes. For example, as shown in SEM images in Fig. 6b, good bonding between layers without any pores

could be observed, while un-melted particles and pores may be induced during the material melting and solidification processes in selective laser sintering if the processing parameters are not well optimised [30, 31]. The ratio of the maximum measured temperature in Fig. 7 to the melting point of the material is around 0.75. This agrees well with previous work [32, 33]. For example, as reported by Garcia et al. [33] using rod-based AFSD, the peak temperature ranged from 49 to 79% of the melting temperature of the Cu bar, while the ratio was 76–92% for Al–Si–Mg bar, for which the difference was attributed to the decrease rate of the yield strength as temperature increases. It should be noted that the measured temperature corresponds to the material at the outermost side of the layer in the depositing state, which is smaller than the highest temperature of the material close to the centre of the tool.

Figure 6a also shows that there are no significant depressions or bulges on the skin of the specimen, indicating a relative uniformity of heat generation and flow during the deposition process. There are small ripples along the length direction of the specimen, which are also called “onion rings” in rod-based AFSD by Lopz et al. [34] and Perry et al. [35]. The corresponding zoomed-out image of the ripple skin is shown in Fig. 6c, in which the arrows in green and orange colour represent the advancing and rotational direction of the tool. It is clearly found that the contour of the ripples is consistent with the moving direction of the tool, i.e. the orientation and the circular direction of the ripples are the same as the advancing and rotational directions of the tool, respectively. The formation of the ripples observed in this work is attributed to the same mechanism as that observed in rod-based AFSD, i.e. the interaction between the tool edge and the top surface of the depositing layer during each revolution of the tool, as summarised by Perry et al. [35]. As the tool moves forward, the top part of the deposited material would flow out of the friction stir zone from the trailing side, and the trailing edge of the tool effectively mills an imprint into the deposited material.

The naked-eye observation of the specimen on the lateral side is shown in Fig. 9. Typical flashes occur at the edge of the specimens along the advancing direction of the tool, as outlined by the orange box. This kind of defect could also be found in other types of AFSD methods, such as the rod-based AFSD as reported in Patil et al. [36] using IN625 rod and Joshi et al. [9] using AZ31B Mg alloy rod. Here, the flash is mainly due to the instability of the flow of the softened material. The amount of extruded material from the gap between the tool and the work surface is not stable to some extent during the deposition process. This instability is mainly due to the complex mechanical interaction between the powder material and the tool, resulting in variation in the stress of the material flow. Meanwhile, the instability could also be induced by the heating process of the powder

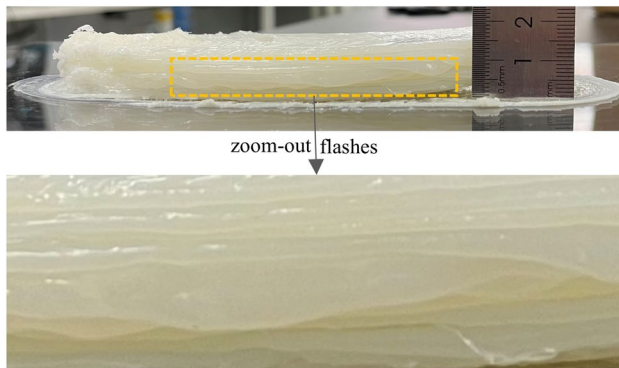


Fig. 9 Lateral view of the specimen, in which edge flashes could be observed

material from the friction stir effects of the tool as well as the cooling process of softened material from the previously deposited layer and atmosphere, which induces the variation of the viscosity of the material. When the tool extrudes too much material, the excess material would flow outside the edges of the specimens. This could be observed from Fig. 10 and the corresponding video shown in supplementary materials, as obtained by using a high-speed camera. Of course, these common AFSD defects, such as ripple skin and edge flashes, may be reduced through the coupling control of the mechanical effect and the heat due to friction stir, which was reported by Merritt et al. [37] for rod-based AFSD of aluminium alloy 6061.

Figure 10 also shows that even when the material is extruded from the channel between protrusions of the tool, it could continue to flow due to the shear action of the bottom surface of the tool shoulder, which can be clearly

observed from the orange outlines in Fig. 10. By analysing Fig. 10a–c using ImageJ software [38], the velocity of the material flow in the rotational direction could be roughly estimated by tracking the front of the material flow, i.e. the rightmost point of the orange outlines in Fig. 10. It is around 2–3 mm/s, which is much smaller than the rotational speed of the tool (e.g. 2 m/s at the outmost edge of tool protrusions). It should be noted that this velocity corresponds to the material flow at the outmost position of the rotating tool protrusions instead of the ones in the inner stir friction region. This is intuitively expected as the material has already been cooled down to some extent as soon as it is extruded from the channel between tool protrusions. Under this condition, the material behaves as a semi-fluid at very high viscosity, resulting in a large resistance to flow and a large loss of kinetic energy of the material flow. Thereby, the material at the outer edge of the rotating tool flows at a much slower velocity than the tool. This phenomenon also exists in the rod-based AFSD of metal materials. For example, as reported by Sharma et al. [32], the velocity of the material flow at the outer edge of the rotating tool was around 1.76 mm/s, while the maximum tip speed of the tool was 0.8 m/s.

3.2 Thermodynamic and mechanical performance

The thermodynamic property of the specimen is characterised by a differential scanning calorimeter (DSC 6000, PerkinElmer, Inc, USA), including the primary melting, crystallisation transformation, and second melting behaviour. Under a nitrogen atmosphere, the specimen is heated from 25 °C to 300 °C (first heating) at a heating rate of 10 °C/min, held for 3 min at 300 °C to eliminate residual crystals, and then cooled to 25 °C (first cooling) at a cooling rate of

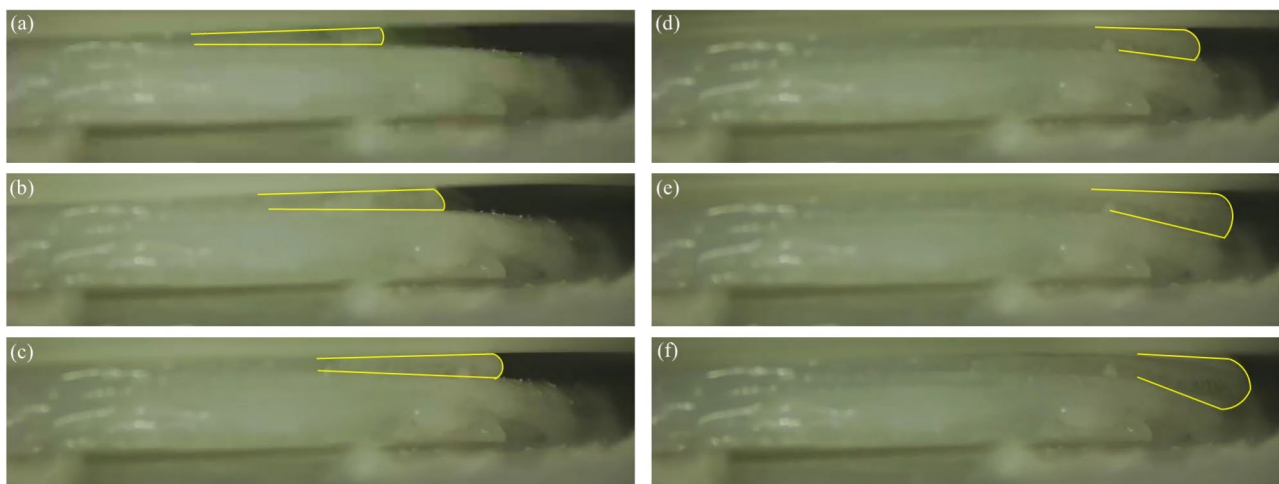


Fig. 10 The flow of materials at the gap between the rotating tool and worksurface, for which the pictures shown in a–f are sequentially arranged, and time interval between two adjacent pictures is 0.8 s, and the orange outlines are used for a clear illustration of the material flow

10 °C/min, held for 1 min at 25 °C. These procedures are followed by heating the specimen up to 300 °C again at the same heating rate to measure the second melting behaviour (second heating). The characteristic curve of the variation of the normalised heat flow with the temperature is shown in Fig. 11, where the curves of the original powder are given as an example, and the heat release direction is represented by a downward arrow. The curves are analysed by using Advantage software (TA Instruments, USA). Figure 11 shows that for the original powder, the latent heat released during the primary melting is much larger than that during the second melting. Based on the first heating and cooling curves, the initial and final melting/crystallisation temperature could be determined by the intersections of two lines tangent to the two steepest sections of the melting/crystallisation peak with the baseline. Table 3 summarises the thermodynamic properties during the primary melting and crystallisation processes for the powder and the manufactured specimens, where the standard deviation of the characterisation results of different samples is also included for each specimen. It could be found that for the original powder, the latent heat in the heating process is much larger than the ones in the

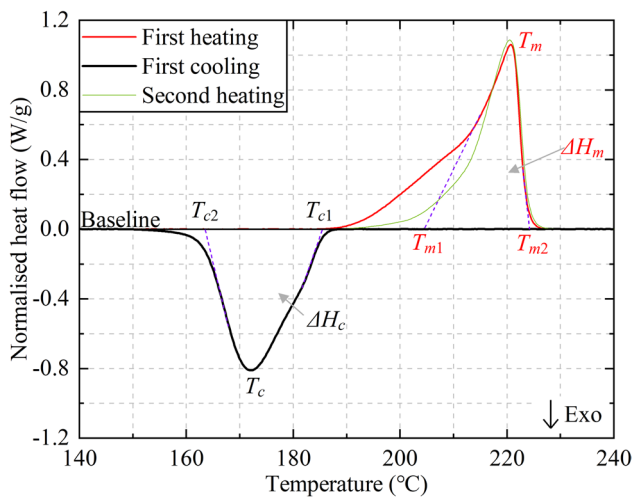


Fig. 11 Characteristic curve of the variation of the normalised heat flow with the temperature as measured by differential scanning calorimeter, where the curves of original powder are given as an example

crystallisation process. However, for the specimens manufactured in this work, the melting latent is close to that of the crystallisation latent. With the increase of the particle size (i.e. d_{50} = 0.258, 0.488, 0.791 mm for specimens A, B and C, respectively), the melting enthalpy of the corresponding specimen increases slightly. For other thermodynamic properties, they do not show a significant difference between different kinds of specimens.

To further investigate the crystallisation behaviour of the specimens, X-ray diffraction (XRD) analysis is conducted by using MiniFlex 600 (Rigaku Corporation, Japan), and the results are shown in Fig. 12, in which the collection range is 5–90° and the step size is 5°/min. The original powder exhibits two prominent crystal diffraction peaks observed at 2θ = 20.15° and 2θ = 23.93° (d -spacing of 0.44 nm and 0.37 nm, respectively). These peaks correspond to the α -type crystals, i.e. α_1 (200) and α_2 (020). This is consistent with the thermodynamic properties as measured by DSC, in which the powder exhibits a single melting peak with a relatively high melting enthalpy, indicating the presence of α -type crystals. It is well known that nylon 6 mainly crystallises as α -type and γ -type crystals, depending on the processing parameters. Meanwhile, α -type crystals are

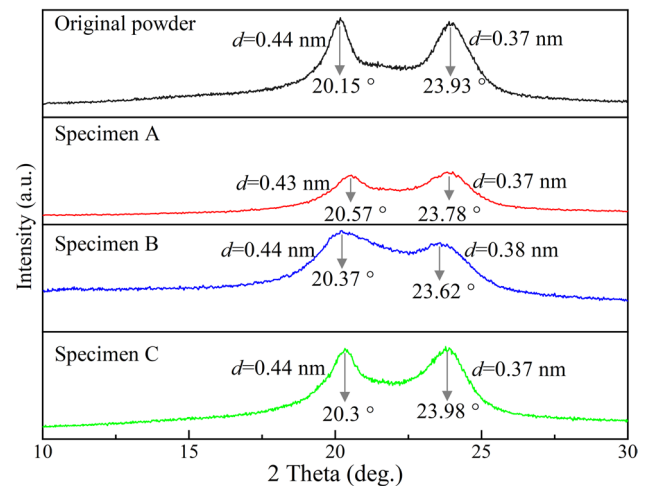


Fig. 12 XRD patterns of the original powder and specimens manufactured from different kinds of powder

Table 3 Melting and crystallisation thermodynamic properties of the original powder and manufactured specimens, as measured by differential scanning calorimeter

Samples	Melting enthalpy ΔH_m (J/g)	Peak melting temperature T_m (°C)	Onset melting temperature T_{m1} (°C)	Crystallisation enthalpy ΔH_c (J/g)	Peak crystallisation temperature T_c (°C)	Onset crystallisation temperature T_{c1} (°C)
Original powder	82.2	221.5	207.6	59.6	174.8	188.0
Specimen A	55.7 ± 1.7	222.4 ± 0.2	211.1 ± 0.1	64.2 ± 2.0	185.9 ± 0.8	189.2 ± 0.2
Specimen B	61.5 ± 2.6	222.4 ± 0.1	208.3 ± 0.7	60.6 ± 4.1	185.5 ± 0.3	189.2 ± 0.1
Specimen C	63.4 ± 2.7	220.2 ± 0.7	207.4 ± 2.2	62.7 ± 3.6	173.1 ± 3.5	185.3 ± 4.4

more thermodynamically stable and usually indicate better mechanical properties compared to that of γ -type crystals. The XRD patterns of the specimens manufactured from different kinds of powder (i.e. powders A-C) all show the same behaviour as that of the original powder, i.e. only α -type crystals, and there is no presence of γ -type crystals, confirming the results of DSC. It should be noted that all specimens manufactured in this work are under natural cooling conditions at room temperature, and there are no actions to control the temperature of the surrounding atmosphere of the specimen or the substrate. This is much different to the situations found in selective laser sintering, in which γ -type crystals could only be avoided when the temperature of the powder bed or the chamber is accurately controlled, as reported by Chen et al. [39] and Salmoria et al. [40].

The mechanical behaviour of the specimen, i.e. hardness, is characterised by the nano-indentation technique, using Hysitron TI-950 Nanoindenter (Hysitron, Inc, USA). The indenter is a triangular pyramid Berkovich diamond indenter with an angle between the centreline and the cone of 65.03° . The specimens are tested with a maximum normal load of 10 mN and a loading/unloading rate of 20 mN/min. The maximum normal load is held for 10 s at the end of the loading stage. Typical curves of the variation of the load with the displacement are shown in Fig. 13. It can be observed that with the increase of particle size of the powder (i.e. $d_{50}=0.258, 0.488$, and 0.791 mm for specimens A, B and C, respectively), both the loading and unloading curves of the corresponding specimen gradually move to the left, i.e. larger normal load is required at the same penetration depth of the indenter. It suggests that the specimen manufactured from the powder with a larger particle size is more resistant to deformation. Meanwhile, the creep displacement at the holding stage of the maximum load shows a similar trend. It is 105 nm, 78 nm and 76 nm for specimens A, B and C, respectively, suggesting that specimen A, manufactured from the finest powder, is relatively weaker than specimens B and C.

The hardness of the specimen is shown in Fig. 14, which is calculated by using the Oliver–Pharr rule [41]. It can be observed that with the increase of the particle size of the powder, the hardness of the corresponding specimen increases. For example, for specimen A, as manufactured from the powder with $D_{50}=0.258$ mm, the hardness is 162 MPa, while for specimen C, as manufactured from the powder with $D_{50}=0.791$ mm, the hardness is 197 MPa. The large hardness of the specimen reported in this work may be attributed to the stable α -type crystals found in the specimen as described above. These values are larger than the ones reported in previous articles using other manufacturing methods, demonstrating the advantages of recycling nylon 6 powder using AFSD. For example, the Vickers hardness of the specimen using hot press moulding of nylon 6 powder

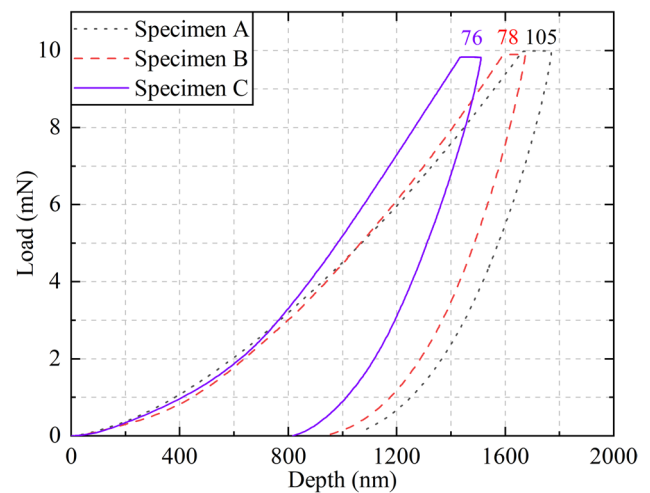


Fig. 13 Typical curves of the variation of the force with the displacement as measured by using the nano-indentation technique, in which specimens A, B and C are manufactured from the powder with $d_{50}=0.258, 0.488, 0.791$ mm, respectively

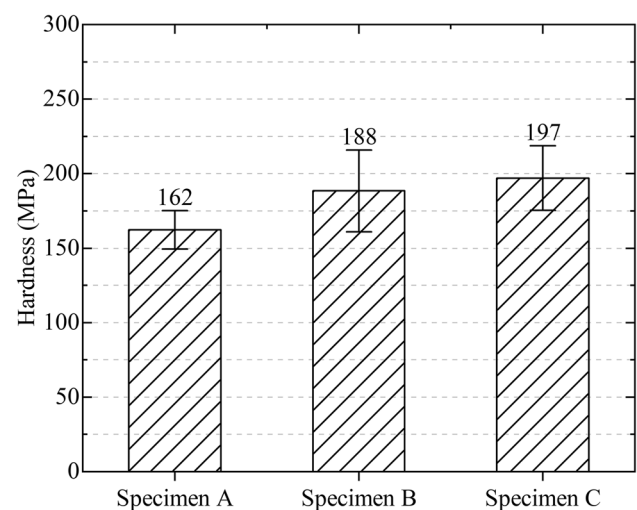


Fig. 14 Hardness of different specimens as measured by nano-indentation tests

with 200 mesh size ($75\ \mu\text{m}$) is 13.01 HV (127.58 MPa), as reported by Huang et al. [42], and the nanoindentation hardness of the specimen using injection moulding of nylon 6 pellets is maximum 92 MPa, as reported by Shen et al. [43], while the ball indentation hardness of the nylon 6 (product 6 XAU) from ERTALON™ is 165 MPa, as reported by Toth et al. [44].

The difference in hardness among the specimens, particularly the significant difference between specimen A and specimen C, is likely attributable to the interaction between the tool and powder during the deposition process, which could be described by the temperature of the material

between the tool and the worksurface as measured by the infrared thermal imager, as shown in Fig. 15. The fluctuation of temperature is the largest for specimen A, while it is smallest for specimen C. It suggests that the particle size of the powder is critical to the deposition process. For the powder with larger particle size, their superior fluidity and greater packing density enable better contact with the rotating tool, leading to a more significant friction stir effect between the tool's protrusion and the particles. Consequently, the plastic deformation of the particles becomes more intense and uniform. Moreover, substantial temperature fluctuations can alter the cooling rate and thermal contraction behaviour of the specimen, which may also have effects on the hardness. Figure 15 also shows that the average temperature is almost the same for all specimens, demonstrating again the feasibility of controlling the deposition temperature in the manufacturing method developed in this work.

4 Conclusions

A novel powder-based additive friction stir deposition (AFSD) with coaxial powder feeding is proposed in this work, and its feasibility in the recycling of nylon 6 powder with different size classes is demonstrated. The concepts and details of this manufacturing method are described, and the quality and performance of the manufactured specimen are examined, including the temperature and flow pattern of the material during the deposition process and the hardness as measured by nanoindentation as well as crystal structure as measured by XRD. The

main results from the present study are summarised as follows:

- (1) A novel powder-based additive friction stir deposition (AFSD) with coaxial powder feeding is proposed, in which the material can be continuously fed by a screw, and it has a very low requirement on the particle size. The plastic deformation of powder material is mainly due to the friction stir effect of the rotating tool instead of the screw extrusion, which could avoid blocking and jamming at the outlet of the funnel and expand the mode of raw material delivery in the AFSD process.
- (2) The manufactured specimen has no significant defects except for the ripple skin and flashes at the edges, which are also prone in other kinds of AFSD. The deposition temperature of the powder material is around 75% of the melting temperature. The material extruded from the channel between the protrusions of the tool moves at a very slow speed before being deposited onto the base, which is only a few percent of the rotational speed of the tool.
- (3) The thermodynamic properties and the crystal structure of the specimen are not sensitive to the particle size of the powder. The hardness of the specimen corresponding to powders A, B and C is 162, 188 and 197 MPa, respectively. The high hardness of the specimen demonstrates the advantage of the additive friction stir deposition. The mechanical performance of the specimen increases with the particle size of the powder as they are more easily plastically deformed under the friction stir effect of the tool.

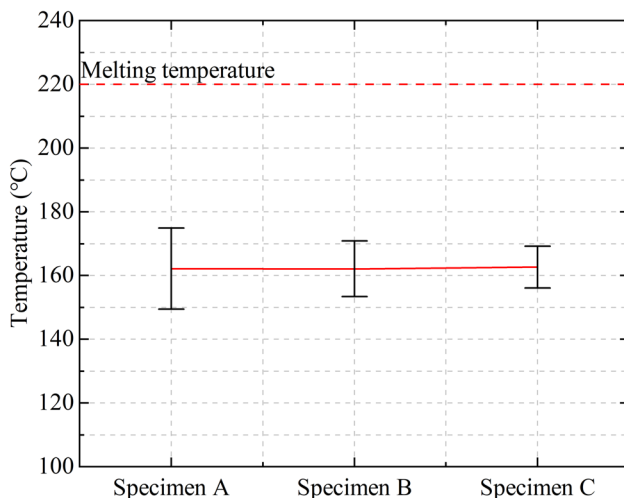


Fig. 15 The peak temperature of the material layer between the tool and the worksurface as measured by the infrared thermal imager during the deposition process, where the error bars indicate the minimum and maximum value of the peak temperature

Supplementary Information The online version contains supplementary material available at <https://doi.org/10.1007/s40964-025-01161-x>.

Acknowledgements The authors are grateful to the National Natural Science Foundation of China (Grant No. U2241248). The first author is thankful to Mr Lanzhou Ge and Mr Wenbin Xuan for their support and help in the set-up of the experiment, and the first corresponding author is thankful to Prof. Mojtaba Ghadiri, University of Leeds, UK, for his inspiration on the application of powder technology to additive manufacturing. All authors reviewed the manuscript.

Author contributions Liu and Nan collaboratively established the experimental setup, processed the data, and drafted the manuscript. Nan also took responsibility for reviewing the manuscript. Both Liu and He conducted the experiment together. Sun and Li provided financial support.

Funding This research was funded by National Natural Science Foundation of China, Grant no [U2241248].

Data availability No datasets were generated or analysed during the current study.

Declarations

Conflict of interest The authors declare no competing interests.

References

- Mason CJT, Rodriguez RI, Avery DZ, Phillips BJ, Bernarding BP, Williams MB, Cobbs SD, Jordon JB, Allison PG (2021) Process-structure-property relations for as-deposited solid-state additively manufactured high-strength aluminum alloy. *Addit Manuf* 40:101879
- Khodabakhshi F, Gerlich AP (2018) Potentials and strategies of solid-state additive friction-stir manufacturing technology: a critical review. *J Manuf Process* 36:77–92
- Akbari M, Aliha MRM, Berto F (2023) Investigating the role of different components of friction stir welding tools on the generated heat and strain. *Forces Mech* 10:100166
- Akbari M, Khalkhali A, Keshavarz SME, Sarikhani E (2015) Investigation of the effect of friction stir processing parameters on temperature and forces of Al–Si aluminum alloys. *Proc Inst Mech Eng Part L* 232(3):213–229
- Shamsaei N, Yadollahi A, Bian L, Thompson SM (2015) An overview of direct laser deposition for additive manufacturing; Part II: Mechanical behavior, process parameter optimization and control. *Addit Manuf* 8:12–35
- Agrawal P, Haridas RS, Yadav S, Thapliyal S, Gaddam S, Verma R, Mishra RS (2021) Processing-structure-property correlation in additive friction stir deposited Ti-6Al-4V alloy from recycled metal chips. *Addit Manuf* 47:102259
- Yaknesh S, Rajamurugu N, Prakash KB, Raju RK, Saleel CA, Rajendran P, Lee IE, Arputharaj BS (2024) A critical review on the performance and microstructural characteristics of materials fabricated through friction stir additive methods and deposition techniques. *J Mater Res Technol* 33:8002–8024
- Avery DZ, Cleek CE, Phillips BJ, Rekha MY, Kinser RP, Rao HM, Brewer LN, Allison PG, Jordon JB (2022) Evaluation of microstructure and mechanical properties of Al–Zn–Mg–Cu alloy repaired via additive friction stir deposition. *J Eng Mater Technol*. <https://doi.org/10.1115/1.4052816>
- Joshi SS, Patil SM, Mazumder S, Sharma S, Riley DA, Dowden S, Banerjee R, Dahotre NB (2022) Additive friction stir deposition of AZ31B magnesium alloy. *J Magnes Alloys* 10(9):2404–2420
- Martin LP, Luccitti A, Walluk M (2022) Evaluation of additive friction stir deposition of AISI 316L for repairing surface material loss in AISI 4340. *Int J Adv Manuf Technol* 121(3–4):2365–2381
- Chen H, Zou N, Xie Y, Meng X, Ma X, Wang N, Huang Y (2025) Wire-based friction stir additive manufacturing of Al Cu alloy with forging mechanical properties. *J Manuf Process* 133:354–366
- Zhang M, Jiang T, Feng X, Xie Y, Su Y, Sun Z, Wang W, Xu Y, Li W (2024) Investigation on in-situ tensile behaviors of 6061 aluminum alloy fabricated by wire additive friction stir deposition. *J Alloys Compd* 1008:176780
- Aghajani Derazkola H, Khodabakhshi F, Gerlich AP (2020) Friction-forging tubular additive manufacturing (FFTAM): a new route of solid-state layer-upon-layer metal deposition. *J Mater Res Technol* 9(6):15273–15285
- Derazkola HA, Khodabakhshi F, Gerlich AP (2020) Fabrication of a nanostructured high strength steel tube by friction-forging tubular additive manufacturing (FFTAM) technology. *J Manuf Process* 58:724–735
- Chaudhary B, Jain NK, Murugesan J, Patel V (2022) Exploring temperature-controlled friction stir powder additive manufacturing process for multi-layer deposition of aluminum alloys. *J Market Res* 20:260–268
- Chaudhary B, Jain NK, Murugesan J, Patel V (2023) Friction stir powder additive manufacturing of Al 6061 alloy: Enhancing microstructure and mechanical properties by reducing thermal gradient. *J Market Res* 26:1168–1184
- Chen H, Meng X, Chen J, Xie Y, Wang J, Sun S, Zhao Y, Li J, Wan L, Huang Y (2023) Wire-based friction stir additive manufacturing. *Addit Manuf* 70:103557
- Zhang Z, Wan L, Meng X, Xie Y, Tian H, Mao D, Dong W, Sun X, Ma X, Huang Y (2024) Robotic wire-based friction stir additive manufacturing. *Addit Manuf* 88:104261
- Jordon JB, Allison PG, Phillips BJ, Avery DZ, Kinser RP, Brewer LN, Cox C, Doherty K (2020) Direct recycling of machine chips through a novel solid-state additive manufacturing process. *Mater Des* 193:108850
- Beck SC, Williamson CJ, Kinser RP, Rutherford BA, Williams MB, Phillips BJ, Doherty KJ, Allison PG, Jordon JB (2023) Examination of microstructure and mechanical properties of direct additive recycling for Al–Mg–Mn alloy Machine chip waste. *Mater Des* 228:111733
- Zhang M, Jiang T, Sun Z, Feng S, Ma L, Wang W, Su Y, Xu Y, Li W (2025) Screw-fed powder-based additive friction stir deposition: a study on pure aluminum. *J Mater Process Technol* 337:118730
- Chaudhary B, Jain NK, Murugesan J (2022) Development of friction stir powder deposition process for repairing of aerospace-grade aluminum alloys. *CIRP J Manuf Sci Technol* 38:252–267
- Mukhopadhyay A, Saha P (2020) Mechanical and microstructural characterization of aluminium powder deposit made by friction stir based additive manufacturing. *J Mater Process Technol* 281:116648
- Chaudhary B, Patel M, Jain NK, Murugesan J, Patel V (2023) Friction stir powder additive manufacturing of Al 6061/FeCoNi and Al 6061/Ni metal matrix composites: reinforcement distribution, microstructure, residual stresses, and mechanical properties. *J Mater Process Technol* 319:118061
- Mukhopadhyay A, Saha P, Singh PK, Verma M (2023) Development and analysis of a powder bed friction stir (PBFS) additive manufacturing process for aluminum alloys: a study on friction-stirring pitch (ω/v) and print location. *Addit Manuf* 72:103618
- Roberts AW (1999) The influence of granular vortex motion on the volumetric performance of enclosed screw conveyors. *Powder Technol* 104:56–67
- Nan W, Xuan W, He Z, Hou H, Sun Z, Li W (2025) Analysis of the screw feeding process in powder-based additive friction stir deposition. *Powder Technol* 455:120791
- Mishra RS, Haridas RS, Agrawal P (2022) Friction stir-based additive manufacturing. *Sci Technol Weld Join* 27(3):141–165
- Mukhopadhyay A, Saha P (2022) A critical review on process metrics–microstructural evolution–process performance correlation in additive friction stir deposition (AFS-D). *J Brazil Soc Mech Sci Eng*. <https://doi.org/10.1007/s40430-022-03729-y>
- Calignano F, Giuffrida F, Galati M (2021) Effect of the build orientation on the mechanical performance of polymeric parts produced by multi jet fusion and selective laser sintering. *J Manuf Process* 65:271–282
- Yang F, Zobeiry N, Mamidala R, Chen X (2023) A review of aging, degradation, and reusability of PA12 powders in selective laser sintering additive manufacturing. *Mater Today Commun* 34:104
- Sharma S, Mani Krishna KV, Radhakrishnan M, Pantawane MV, Patil SM, Joshi SS, Banerjee R, Dahotre NB (2022) A pseudo thermo-mechanical model linking process parameters to microstructural evolution in multilayer additive friction stir deposition of magnesium alloy. *Mater Des* 224:111412
- Garcia D, Hartley WD, Rauch HA, Griffiths RJ, Wang R, Kong ZJ, Zhu Y, Yu HZ (2020) In situ investigation into temperature

- evolution and heat generation during additive friction stir deposition: A comparative study of Cu and Al-Mg-Si. *Addit Manuf* 34:101368
34. Lopez JJ, Williams MB, Rushing TW, Confer MP, Ghosh A, Griggs CS, Jordon JB, Thompson GB, Allison PG (2022) A solid-state additive manufacturing method for aluminum-graphene nanoplatelet composites. *Materialia* 23:101440
 35. Perry MEJ, Griffiths RJ, Garcia D, Sietins JM, Zhu Y, Yu HZ (2020) Morphological and microstructural investigation of the non-planar interface formed in solid-state metal additive manufacturing by additive friction stir deposition. *Addit Manuf* 35:101293
 36. Patil SM, Krishna KVM, Sharma S, Joshi SS, Radhakrishnan M, Banerjee R, Dahotre NB (2024) Thermo-mechanical process variables driven microstructure evolution during additive friction stir deposition of IN625. *Addit Manuf* 80:103958
 37. Merritt GR, Williams MB, Allison PG, Jordon JB, Rushing TW, Cousin CA (2022) Closed-loop temperature and force control of additive friction stir deposition. *J Manuf Mater Process* 6(5):92
 38. Johannes S, Ignacio A-C, Erwin F, Verena K, Mark L, Tobias P, Stephan P, Curtis R, Stephan S, Benjamin S, Jean-Yves T, James WD, Volker H, Kevin E, Pavel T, Albert C (2012) Fiji: an open-source platform for biological-image analysis. *Nat Methods* 9(7):676–682
 39. Chen P, Wu H, Zhu W, Yang L, Li Z, Yan C, Wen S, Shi Y (2018) Investigation into the processability, recyclability and crystalline structure of selective laser sintered Polyamide 6 in comparison with Polyamide 12. *Polym Test* 69:366–374
 40. Salmoria GV, Leite JL, Paggi RA (2009) The microstructural characterization of PA6/PA12 blend specimens fabricated by selective laser sintering. *Polym Test* 28(7):746–751
 41. Oliver WC, Pharr GM (1992) An improved technique for determining hardness and elastic modulus using load and displacement sensing indentation experiments. *J Mater Res* 7(6):1564–1583
 42. Huang S-J, Tanoto YY, Li C (2025) Effect of powder mixing on the mechanical strength of polyamide 6-AZ61 magnesium composites prepared by compression molding. *Composites Commun* 53:102169
 43. Shen L, Phang IY, Liu T (2006) Nanoindentation studies on polymorphism of nylon 6. *Polym Testing* 25(2):249–253
 44. Tóth LF, Sukumaran J, Szebényi G, De Baets P (2019) Tribomechanical interpretation for advanced thermoplastics and the effects of wear-induced crystallization. *Wear* 440:203083

Publisher's Note Springer Nature remains neutral with regard to jurisdictional claims in published maps and institutional affiliations.

Springer Nature or its licensor (e.g. a society or other partner) holds exclusive rights to this article under a publishing agreement with the author(s) or other rightsholder(s); author self-archiving of the accepted manuscript version of this article is solely governed by the terms of such publishing agreement and applicable law.